Supplemental Material for "Probing time reversal symmetry breaking topological superconductivity in twisted double layer copper oxides with polar Kerr effect"

Oguzhan Can,[1] Xiao-Xiao Zhang,[1,2] Catherine Kallin,[3] and Marcel Franz[1]

[1]*Department of Physics and Astronomy & Stewart Blusson Quantum Matter Institute, University of British Columbia, Vancouver BC, Canada V6T 1Z4*
[2]*RIKEN Center for Emergent Matter Science (CEMS), Wako, Saitama 351-0198, Japan*
[3]*Department of Physics and Astronomy, McMaster University, Hamilton, ON, Canada L8S 4M1*

(Dated: March 24, 2021)

DETAILS ON THE 2-BAND MODEL

In this section we give a derivation of the 2-band model discussed in the main text. We assume the regime of strong hole doping such that the Fermi surface is small and confined to the center of the Brillouin zone Γ. While this may be relevant for strongly overdoped $Bi_2Sr_2CaCu_2O_{8+\delta}$ the primary goal of this derivation is to obtain a simple, analytically tractable model, that will provide insights into the physics of the Hall conductivity in the general class of twisted bilayer d-wave superconductors.

To construct the 2-band model we employ the following strategy. We begin from two initially decoupled CuO_2 layers described as BCS d-wave superconductors. We expand the electron dispersions and gap functions to leading order in small momentum k around the Γ point and perform a rotation by angle $\pm\theta/2$ in the two layers. Next we regularize these expressions on two perfectly aligned (i.e. unrotated) square lattices with the lattice constant b given by the moiré unit cell and write down the corresponding tight-binding model. Finally we couple the two layers by a generic single-electron tunneling $g(\boldsymbol{k})$ consistent with the system symmetries. The final 2-band model is thus defined on a pair of aligned square lattices with the twist encoded in the effective dispersion relations and gap functions.

d+id case. – Starting with two decoupled CuO_2 planes we expand the dispersion of each monolayer near the BZ center, keeping terms up to $\mathcal{O}(k^4)$

$$\begin{aligned}\epsilon_k &= -2t(\cos k_x a + \cos k_y a) \qquad \text{(S1)}\\ &\simeq -2t\left[2 - \frac{1}{2}k^2a^2 + \frac{1}{8}k^4a^4 - \frac{1}{16}(2k_xk_y)^2a^4\right].\end{aligned}$$

The fourth order terms are required to capture the 4-fold anisotropy of the dispersion which, as we shall see, turns out to be important for the Hall response. The pair functions are expanded to second order

$$\Delta_k = \frac{\Delta_0}{2}(\cos k_x a - \cos k_y a) \simeq -\frac{\Delta_0}{4}(k_x^2 - k_y^2)a^2. \qquad \text{(S2)}$$

Now we account for the twist by counter-rotating each layer by angle $\pm\theta/2$ as shown in Fig. S1. Under a rotation by $\theta/2$ various terms transform as

$$k_x^2 - k_y^2 \to (k_x^2 - k_y^2)\cos\theta + (2k_xk_y)\sin\theta,$$

$$2k_xk_y \to (2k_xk_y)\cos\theta - (k_x^2 - k_y^2)\sin\theta.$$

Next we construct a tight binding model whose low-energy expansion near the Γ point gives the above rotated dispersion relation and gap functions. This is achieved by replacing

$$k_x a \to \frac{a}{b}\sin(k_x b), \quad (k_x a)^2 \to \frac{2a^2}{b^2}[1 - \cos(k_x b)],$$

and similar for k_y. Here b is the lattice constant of the moiré lattice that results from the twisted geometry (we assume commensurate twist angle θ). We thus obtain

$$\begin{aligned}\xi_k(\theta) = &-\mu - 4t\left(1 - a^2/b^2\right) \qquad \text{(S3)}\\ &- 2t\Bigg[\frac{a^2}{b^2}(\cos k_x b + \cos k_y b)\\ &- \frac{1}{4}\frac{a^4}{b^4}\left(\eta_{xy}\cos\theta + \eta_{x^2-y^2}\sin\theta\right)^2\Bigg],\end{aligned}$$

and the pairing

$$\Delta_k(\theta) = \frac{\Delta_0}{2}\frac{a^2}{b^2}\left[\eta_{x^2-y^2}\cos\theta - \eta_{xy}\sin\theta\right], \qquad \text{(S4)}$$

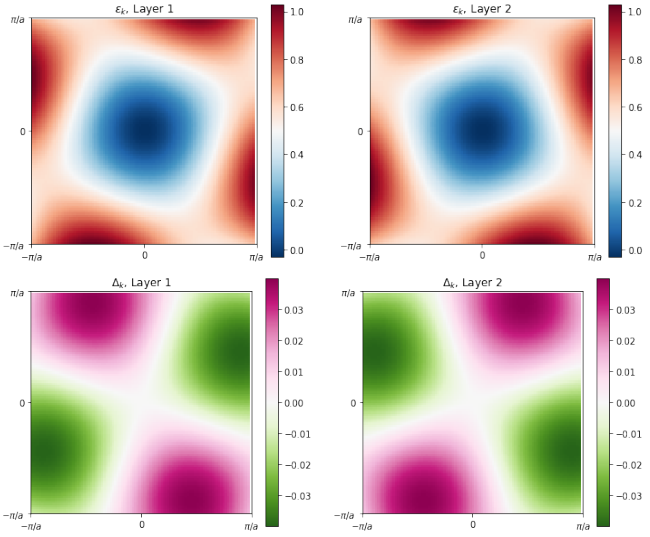

FIG. S1. Normal parts of energy dispersions (top) and the order parameter (bottom) for decoupled layers that are naively rotated by $\pm\theta/2$ with $\theta = 2\arctan(1/2)$. We observe that the the patterns are no longer periodic when plotted in the original Brillouin zone.

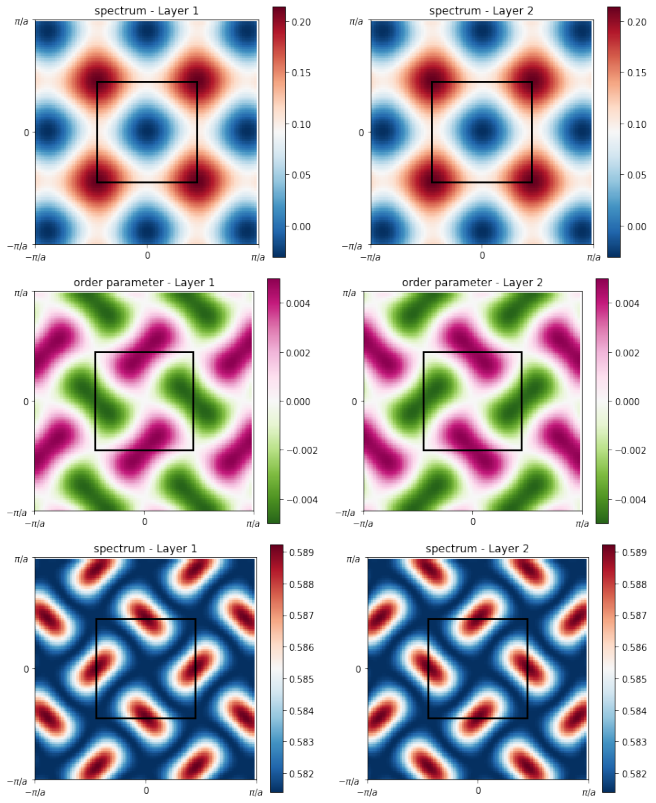

FIG. S2. Normal state dispersion (top) and order parameter (middle) of the effective 2-band model constructed for $\theta = 2\arctan(1/2)$. The black square encloses the moiré unit cell with length $2\pi/b$ and we observe that the patterns are now properly periodic. The last term in Eq. (S3) is plotted separately (bottom row) as it is very small compared to the other terms. However, inclusion of this term is very important since without it we would have $\xi_1 = \xi_2$ and the Hall conductivity would identically vanish.

where

$$\eta_{xy} = \sin k_x b \sin k_y b, \tag{S5}$$
$$\eta_{x^2-y^2} = \cos k_x b - \cos k_y b. \tag{S6}$$

The resulting dispersions can be seen in Fig. S2.

If we define $\tilde{\mu} = \mu + 4t\left(1 - a^2/b^2\right)$, $\tilde{t} = ta^2/b^2$, $\tilde{t'} = \frac{t}{2}a^4/b^4$ and $\tilde{\Delta} = \Delta_0(a^2/b^2)$ as the effective parameters, we obtain the 2-band model defined by the BdG Hamiltonian $\mathcal{H} = \sum_{\boldsymbol{k}} \Psi^\dagger_{\boldsymbol{k}} h^{\text{eff}}_{\boldsymbol{k}} \Psi_{\boldsymbol{k}}$ with

$$h^{\text{eff}}_{\mathbf{k}} = \begin{pmatrix} \xi_1(\boldsymbol{k}) & \Delta_1(\boldsymbol{k}) & g(\boldsymbol{k}) & 0 \\ \Delta_1(\boldsymbol{k})^* & -\xi_1(\boldsymbol{k}) & 0 & -g(-\boldsymbol{k})^* \\ g(\boldsymbol{k})^* & 0 & \xi_2(\boldsymbol{k}) & \Delta_2(\boldsymbol{k}) \\ 0 & -g(-\boldsymbol{k}) & \Delta_2(\boldsymbol{k})^* & -\xi_2(\boldsymbol{k}) \end{pmatrix} \tag{S7}$$

and the Nambu spinor $\Psi_{\boldsymbol{k}} = (c_{\boldsymbol{k}\uparrow 1}, c^\dagger_{-\boldsymbol{k}\downarrow 1}, c_{\boldsymbol{k}\uparrow 2}, c^\dagger_{-\boldsymbol{k}\downarrow 2})^T$.

The effective dispersions and gap functions are given by

$$\xi_{1(2)}(\boldsymbol{k}) = -\tilde{\mu} - 2\tilde{t}(\cos k_x b + \cos k_y b) + \tilde{t'}\left(\eta_{xy}\cos\theta \pm \eta_{x^2-y^2}\sin\theta\right)^2 \tag{S8}$$

$$\Delta_{1(2)}(\boldsymbol{k}) = \frac{\tilde{\Delta}}{2}\left(\eta_{x^2-y^2}\cos\theta \mp \eta_{xy}\sin\theta\right] e^{\pm i\phi/2} \tag{S9}$$

The requisite $\mathcal{T}$ breaking is encoded through the complex phase difference $e^{i\phi}$ between superconducting order parameters in two layers.

In relation to the 10-band model the lattice constant is $b = \sqrt{1^2+2^2}a = \sqrt{5}a$. The corresponding BZ will be smaller, with the dimension $2\pi/b$. The 10-band model can be recovered from the 2-band model by folding the dispersions in Fig. S2 back into the smaller moiré BZ. If we are interested in features that are near the center of the BZ and small enough energies such that they do not backfold, the 2-band model with the above parameters should provide an accurate description.

$d + is$ case. – For the $d + is$ case, the pairing form obtained from self-consistent calculation is

$$\Delta_{1(2)}(k) = \pm\Delta^d \eta_{x^2-y^2} - i\Delta^s\chi \tag{S10}$$

in the local frame of each layer with $\Delta^d = \tilde{\Delta}e^{i\phi/2}\cos\phi/2$, $\Delta^s = \tilde{\Delta}e^{i\phi/2}\sin\phi/2$ and $\chi = \cos k_x b + \cos k_y b$. We can follow the transformation procedure described above to obtain

$$\Delta_{1(2)}(k) = \pm\,\Delta^d(\eta_{x^2-y^2}\cos\theta \mp \eta_{xy}\sin\theta) - i\Delta^s[\chi - \frac{1}{4}(\eta_{xy}\cos\theta \pm \eta_{x^2-y^2}\sin\theta)^2]. \tag{S11}$$

2-band vs. 10-band model results comparison. – In Fig. S3 we contrast our results for $\sigma_H(\omega)$ computed for the two models. We use parameters relevant to the highly overdoped (low filling) regime where we expect some degree of agreement in the optical conductivity between the two models. The tight binding parameters are related as indicated above Eq. (S7). The main difference between the two Hamiltonians is the assumed form of the interlayer couplings. In the 10-band model we assume g_{ij} exponentially decaying with distance as given in Eq. (6) of the main text, while in the 2-band model we use $g(\boldsymbol{k}) = 4g_0\cos(k_x b/2)\cos(k_y b/2)$ corresponding to a nearest neighbor hopping between two monolayers offset by $(b/2, b/2)$. We fix the amplitude of the interlayer coupling in the 10-band model and adjust g_0 in the 2-band model such that the onset frequencies of the $\text{Im}\sigma_H(\omega)$ for two models match. For $g_0^{(10\text{band})} = 8$meV this happens when $g_0^{(2\text{band})} \approx 1.67 g_0^{(10\text{band})}$.

Results in Fig. S3 show that over the entire frequency range the behavior of $\sigma_H(\omega)$ is qualitatively similar in the two models, with the amplitudes differing by about a factor of 2. This level of agreement confirms that the two-band model captures the essential physics of the bilayer system. The discrepancy in the amplitude can be

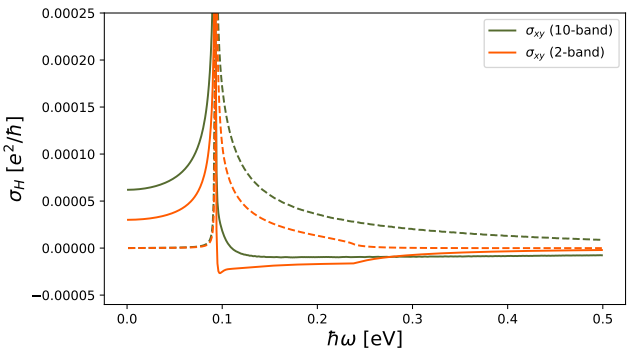

FIG. S3. Comparison of optical Hall conductivities $\sigma_{xy}(\omega)$ between the 2-band (shown in orange) and the 10-band (green) models. Solid and dashed lines show real and imaginary parts respectively. For the 10-band model, tight binding parameters are chosen to be $t = 0.153$eV, $t' = 0$, $\mu = -3.9t$, $\Delta_{\max} = 0.4$eV and $g_0^{(10\text{band})} = 0.008$eV. The phase between monolayers is chosen to be $\phi = 0.4\pi$, breaking the time reversal symmetry. Note that in this plot we calculate the Hall conductance in a different regime and using different parameters (larger order parameter and lower chemical potential compared to the calculations in Fig.1 to show agreement between 2-band and 10-band models.

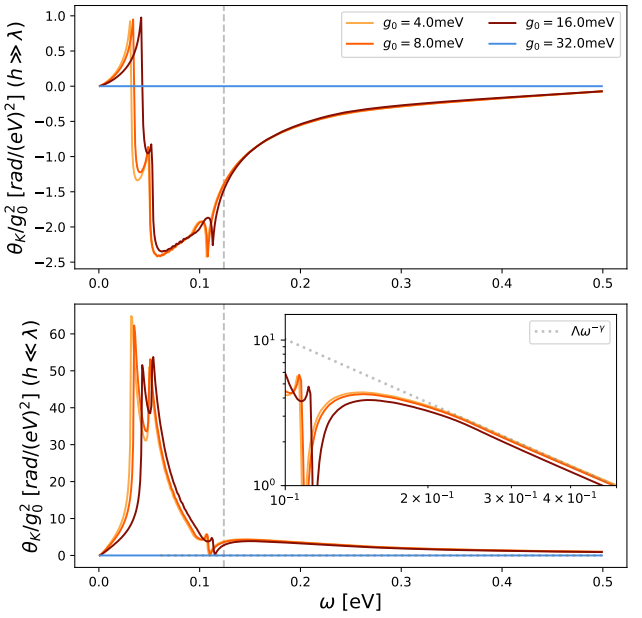

FIG. S4. Scaling collapse of θ_K/g_0^2 indicating leading g_0^2 dependence of the Kerr angle on the interlayer coupling. Top and the bottom panels show thick and thin sample limits, respectively.

attributed to the difference in the form of the interlayer coupling and to the mismatch between the two band structures away from the BZ center.

KERR ANGLE ESTIMATION DETAILS

Material properties – We use data in the Fig. 6 of Ref. [1] to estimate the diagonal part of the optical conductivity $\sigma(\omega)$ of the bulk $Bi_2Sr_2CaCu_2O_{8+\delta}$ near optimal doping. As remarked by the authors the data above $\omega_c = 0.12$ eV is consistent with the power law behaviour $\sigma(\omega) = C(-i\omega)^{\gamma-2}$. The measured quantity is $|\sigma(\omega)| = C\omega^{\gamma-2}$ and we extract the coefficient C and the exponent γ by considering two points on the graph $p_1 = (10^3, 2\times10^3)$ and $p_2 = (10^4, 5.6\times10^2)$ in units of $([\text{cm}^{-1}], [\Omega^{-1}\text{cm}^{-1}])$. We find that $C = 9.122\times10^4\Omega^{-1}(\text{cm}^{-1})^{3-\gamma}$ and $\gamma = 1.447$.

For the index of refraction n appearing in Eq. (1) we use [1]

$$n = \sqrt{\epsilon_H + \frac{i\sigma(\omega)}{\epsilon_0\omega}} \tag{S12}$$

where $\epsilon_H = 4.77$ is the background dielectric tensor. We estimate the 2D conductivity σ_{xx} (required in Eq. 8) from the bulk conductivity through $\sigma = \sigma_{xx}/2d$ where $d = 12.6$Åis the interlayer spacing [2] between Cu-O planes. Note that we consider two Cu-O monolayers in our 2D sample.

Scaling properties of the Kerr angle – Here we discuss the dependence of the Kerr angle on the interlayer coupling strength g_0 and frequency ω focusing specifically on the the experimentally relevant high frequency region. We observe a scaling collapse of the curves in Fig. S4, valid at small g_0, when we plot θ_K/g_0^2 in both thin and thick sample limits. This is consistent with the expected leading quadratic dependence on the interlayer coupling found in the 2-band model.

At high frequencies comparison of Fig. 1 and Eq. (9)

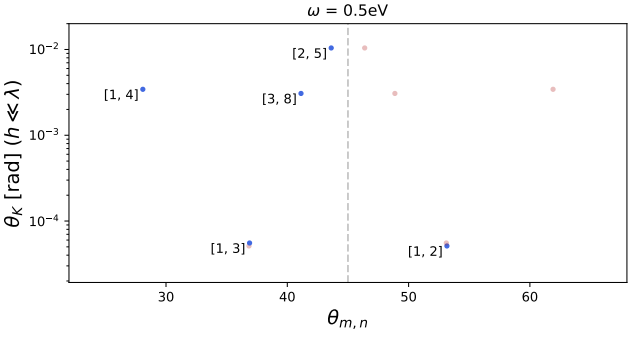

FIG. S5. Kerr angle estimates for other commensurate twist angles $\theta_{m,n}$ at $\omega = 0.5$eV in the thin sample limit ($h \ll \lambda$), annotated by the twist vector $[m, n]$ (blue dots). Each data point is mirrored (red dots) with respect to $\theta_{m,n} = 45^\circ$ to show the expected behaviour for the entire range of twist angles.

indicates that σ_{xy} is smaller than σ_{xx} by at least three orders of magnitude (comparing both real and imaginary parts). It is also true that, at high frequencies $|\mathrm{Re}\sigma_{xy}| \ll |\mathrm{Im}\sigma_{xy}|$ and $\mathrm{Re}\sigma_{xy} \propto \omega^{-2}$. Therefore, in Eq. (8) , it is permissible to neglect σ_{xy} compared to σ_{xx}, which leaves us with

$$\theta_K \simeq \mathrm{Re}\arctan\left(\frac{-\sigma_{xy}}{\sigma_{xx}+4\pi\sigma_{xx}^2}\right). \tag{S13}$$

Because σ_{xx} shows $\propto \omega^{\gamma-2}$ scaling with $\gamma < 2$, at large enough frequencies we can drop the σ_{xx}^2 term as well. Finally, combining the frequency dependences of σ_{xy} and σ_{xx} and noting that $\sigma_{xy}/\sigma_{xx} \ll 1$, we expand $\arctan x \approx x$ for $|x| \ll 1$ and obtain Eq. (10) quoted in the main text. Therein Λ is a prefactor dependent on microscopic details and we included the g_0^2 factor to capture the leading dependence on the interlayer coupling strength observed in Fig. S4.

Results for other commensurate angles — Our lattice model calculations so far focused on a single commensurate twist angle $\theta_{1,2}$. We have also estimated the Kerr angle in the thin sample limit for other commensurate angles which are computationally accessible and Fig. S5 shows these results. We find that the Kerr angle is increased as the twist angle θ approaches 45°. Compared to the $\theta_{1,2}$ case we studied above, $\theta_{2,5} \approx 43°$ configuration results in a θ_K at least two orders of magnitude larger.

OPTICAL HALL CONDUCTIVITY FORMULAS

General multi-band case. – Here we obtain an expression for Hall conductivity in terms of the eigenspectrum of the BdG Hamiltonian $h_{\boldsymbol{k}}|a\boldsymbol{k}\rangle = E^a_{\boldsymbol{k}}|a\boldsymbol{k}\rangle$. It is convenient to define the matrix element $v^x_{a\boldsymbol{k}_1,b\boldsymbol{k}_2} = \langle a\boldsymbol{k}_1|\hat{\mathbf{v}}_x|b\boldsymbol{k}_2\rangle$ and use a collective notation $n = a\boldsymbol{k}_1, m = b\boldsymbol{k}_2$. From Eq. (3) in the main text, we have

$$\begin{aligned}
\pi_{xy}(\boldsymbol{q},\omega) &= \int_0^\infty dt e^{i\omega t}\,\mathrm{tr}\left[\hat{\rho}\,[\hat{j}_x^\dagger(\boldsymbol{q},t),\hat{j}_y(\boldsymbol{q},0)]\right] \\
&= \frac{1}{Z}\int_0^\infty dt e^{i\omega t}\sum_{nml}\left[\langle l|e^{-\beta H}|n\rangle\langle n|\hat{j}_x^\dagger(\boldsymbol{q},t)|m\rangle\langle m|\hat{j}_y(\boldsymbol{q},0)|l\rangle - \langle m|e^{-\beta H}|l\rangle\langle l|\hat{j}_y(\boldsymbol{q},0)|n\rangle\langle n|\hat{j}_x^\dagger(\boldsymbol{q},t)|m\rangle\right] \\
&= i\sum_{mn}\frac{e^{-\beta E_n}-e^{-\beta E_m}}{Z}\frac{\langle n|\hat{j}_x^\dagger(\boldsymbol{q})|m\rangle\langle m|\hat{j}_y(\boldsymbol{q})|n\rangle}{(\omega+i\epsilon)+E_n-E_m} \\
&= ie^2\sum_{\boldsymbol{k},ab} v^{x\dagger}_{a\boldsymbol{k}+\boldsymbol{q},b\boldsymbol{k}} v^y_{b\boldsymbol{k},a\boldsymbol{k}+\boldsymbol{q}}\frac{n_F(E^a_{\boldsymbol{k}})-n_F(E^b_{\boldsymbol{k}+\boldsymbol{q}})}{(\omega+i\epsilon)+E^a_{\boldsymbol{k}}-E^b_{\boldsymbol{k}+\boldsymbol{q}}}
\end{aligned} \tag{S14}$$

In the second line, we use eigenstates $h|n\rangle = E_n|n\rangle$ to express the trace, the partition function $Z = \mathrm{tr}(e^{-\beta h})$, and the density matrix $\hat{\rho} = e^{-\beta h}/Z$. In the third line, we used the time dependence of the current operator $\langle n|\hat{j}_\alpha(t)|m\rangle = \langle n|e^{iht}\hat{j}_\alpha e^{-iht}|m\rangle = e^{i(E_n-E_m)t}\langle n|\hat{j}_\alpha|m\rangle$ and performed the time integral. Noting that $\hat{\mathbf{j}}(\boldsymbol{q}) = e\sum_{a\boldsymbol{k}}(\boldsymbol{k}+\frac{\boldsymbol{q}}{2})c^\dagger_{a\boldsymbol{k}+\boldsymbol{q}}c_{a\boldsymbol{k}}$ shifts the electron momentum by $\boldsymbol{q}$, we immediately see that $\langle n|\hat{j}_\alpha(\boldsymbol{q})|m\rangle = \langle a\boldsymbol{k}_1|\hat{j}_\alpha(\boldsymbol{q})|b\boldsymbol{k}_2\rangle\delta_{\boldsymbol{k}_1,\boldsymbol{k}_2+\boldsymbol{q}}$, which justifies the fourth line. In addition, we identify the Fermi distribution $n_F(E_n)$ with $e^{-\beta E_n}/Z$ because we are dealing effectively with a noninteracting system. For the $\boldsymbol{q}=0$ case of interest, we have $\hat{\mathbf{v}}_\alpha(\boldsymbol{q}=0) = (\mathbb{1}\otimes\sigma_z)\partial_{k_\alpha}h^0_{\boldsymbol{k}}$ in the first quantized form of the original orbital basis, suitable for numerical evaluation.

An alternative way to derive the final expression in Eq. (S14) is to perform an S-matrix expansion of the current-current correlator to one-loop level [3] obtaining

$$\pi_{xy}(\boldsymbol{q},\nu_m) = \frac{ie^2}{\beta}\sum_{\boldsymbol{k},\omega_n}\mathrm{tr}\left[\hat{\mathbf{v}}_x(\boldsymbol{k}+\frac{\boldsymbol{q}}{2})G_0(\boldsymbol{k},\omega_n)\hat{\mathbf{v}}_y(\boldsymbol{k}+\frac{\boldsymbol{q}}{2})G_0(\boldsymbol{k}+\boldsymbol{q},\omega_n+\nu_m)\right] \tag{S15}$$

where $G_0(\boldsymbol{k},\omega_n) = (-i\omega_n + h_{\boldsymbol{k}})^{-1}$ is the Green's function. Expressing G_0 in the spectral representation

$$G_0(\boldsymbol{k},\omega_n) = \int d\omega\frac{\zeta_{\boldsymbol{k}}(\omega)}{-i\omega_n+\omega} \tag{S16}$$

with the matrix $\zeta_{\boldsymbol{k}}(\omega)$ containing all orbital degrees of freedom and substituting into Eq. (S15) we obtain

$$\pi_{xy}(\boldsymbol{q},\nu_m) = ie^2\int d\omega d\nu\sum_{\boldsymbol{k}}\mathrm{tr}\left[\hat{\mathbf{v}}_x\zeta_{\boldsymbol{k}}(\omega)\hat{\mathbf{v}}_y\zeta_{\boldsymbol{k}+\boldsymbol{q}}(\nu)\right]\frac{1}{\beta}\sum_{\omega_n}\frac{1}{i\omega_n-\omega}\frac{1}{i\omega_n+i\nu_m-\nu}.$$

As we evaluate this Matsubara sum, we note that the bosonic Matsubara frequencies $i\nu_m$ appearing in the Fermi function drop out, $n_F(\omega) = n_F(\omega - i\nu_m)$, which leads to

$$\pi_{xy}(\boldsymbol{q}, \nu_m) = ie^2 \int d\omega d\nu \sum_{\boldsymbol{k}} \mathrm{tr}\left[\hat{\mathbf{v}}_x \zeta_{\boldsymbol{k}}(\omega) \hat{\mathbf{v}}_y \zeta_{\boldsymbol{k}+\boldsymbol{q}}(\nu)\right] \frac{n_F(\omega) - n_F(\nu)}{i\nu_m + \omega - \nu}. \tag{S17}$$

Since by definition $U_{\boldsymbol{k}}^\dagger G_0 U_{\boldsymbol{k}} = \hat{\delta}(\omega - E_{\boldsymbol{k}})$ where $[\hat{\delta}(\omega - E_{\boldsymbol{k}})]_{ij} = \delta_{ij}(-i\omega + E^i_{\boldsymbol{k}})^{-1}$, and $U_{\boldsymbol{k}}$ is a unitary matrix that diagonalizes $h_{\boldsymbol{k}}$, we see that $U_{\boldsymbol{k}}^\dagger \zeta_{\boldsymbol{k}}(\omega) U_{\boldsymbol{k}} = \hat{\delta}(\omega - E_{\boldsymbol{k}})$. We use this when inserting the identity $U_{\boldsymbol{k}}^\dagger U_{\boldsymbol{k}} = 1$ into the trace to find

$$\pi_{xy}(\boldsymbol{q}, \nu_m) = ie^2 \int d\omega d\nu \sum_{\boldsymbol{k}} \mathrm{tr}\left[U_{\boldsymbol{k}+\boldsymbol{q}}^\dagger \hat{\mathbf{v}}_x U_{\boldsymbol{k}} \hat{\delta}(\omega - E_{\boldsymbol{k}}) U_{\boldsymbol{k}}^\dagger \hat{\mathbf{v}}_y U_{\boldsymbol{k}+\boldsymbol{q}} \hat{\delta}(\nu - E_{\boldsymbol{k}+\boldsymbol{q}})\right] \frac{n_F(\omega) - n_F(\nu)}{i\nu_m + \omega - \nu}.$$

Taking the trace explicitly and evaluating the integrals with the help of delta functions we obtain the expression on the last line of Eq. (S14) again.

We now write down the Hall conductance in Eq. (2) in the limit $q \to 0$

$$\sigma_H(\omega) = \frac{ie^2}{2\omega} \sum_{\boldsymbol{k},ab} Q_{ab} \frac{n_F(E^a_{\boldsymbol{k}}) - n_F(E^b_{\boldsymbol{k}})}{\omega + E^a_{\boldsymbol{k}} - E^b_{\boldsymbol{k}} + i\epsilon} \tag{S18}$$

where $Q_{ab} = (v^x_{ab} v^y_{ba} - v^y_{ab} v^x_{ba})_{\boldsymbol{k}}$. We may rewrite (S18) as follows

$$\sigma_H(\omega) = \frac{i}{2\omega} e^2 \sum_{\boldsymbol{k},ab} Q_{ab} \frac{n_F(E^a_{\boldsymbol{k}})}{\omega + E^a_{\boldsymbol{k}} - E^b_{\boldsymbol{k}} + i\epsilon} - Q_{ba} \frac{n_F(E^a_{\boldsymbol{k}})}{\omega + E^b_{\boldsymbol{k}} - E^a_{\boldsymbol{k}} + i\epsilon} \tag{S19}$$

$$= \frac{i}{2\omega} e^2 \sum_{\boldsymbol{k},ab} \frac{(Q_{ab} + Q_{ba})(E^a_{\boldsymbol{k}} - E^b_{\boldsymbol{k}}) - (\omega + i\epsilon)(Q_{ab} - Q_{ba})}{(E^a_{\boldsymbol{k}} - E^b_{\boldsymbol{k}})^2 - (\omega + i\epsilon)^2} n_F(E^a_{\boldsymbol{k}}). \tag{S20}$$

which leads to Eq. (4) of the main text once we account for antisymmetry $Q_{ab} = -Q_{ba}$. Hermiticity $v^{x*}_{ab} = v^x_{ba}$ further implies that the antisymmetric quantity $Q_{ab} = 2i\,\mathrm{Im}\{v^x_{ab} v^y_{ba}\}_{\boldsymbol{k}}$ is purely imaginary. The zero-frequency limit of the real part can thus be written as

$$\lim_{\omega \to 0} \sigma_H = -ie^2 \sum_{\boldsymbol{k},ab} \frac{Q_{ab} n_F(E^a_{\boldsymbol{k}})}{(E^a_{\boldsymbol{k}} - E^b_{\boldsymbol{k}})^2 + \epsilon^2}.$$

Explicit formula for the 2-band model. – We start from the general two-band BdG Hamiltonian $h_{\boldsymbol{k}}$ in the following form

$$h_{\boldsymbol{k}} = \begin{pmatrix} \xi_1(\boldsymbol{k}) & \Delta_1(\boldsymbol{k}) & g(\boldsymbol{k}) & 0 \\ \Delta_1^*(\boldsymbol{k}) & -\xi_1(-\boldsymbol{k}) & 0 & -g^*(-\boldsymbol{k}) \\ g^*(\boldsymbol{k}) & 0 & \xi_2(\boldsymbol{k}) & \Delta_2(\boldsymbol{k}) \\ 0 & -g(-\boldsymbol{k}) & \Delta_2^*(\boldsymbol{k}) & -\xi_2(-\boldsymbol{k}) \end{pmatrix}. \tag{S21}$$

Once we assume intralayer inversion symmetry $\xi_i(-\boldsymbol{k}) = \xi_i(\boldsymbol{k})$, it becomes Eq. (S7). Now we have to further specify the relation between $g(\boldsymbol{k})$ and $g(-\boldsymbol{k})$. In general, if we work with interlayer coupling that does not explicitly break $\mathcal{T}$, the complex phase of $g(\boldsymbol{k})$ only enters via the $e^{i(\boldsymbol{r}_{1i} - \boldsymbol{r}_{2j})\cdot\boldsymbol{k}}$ factors (where $\boldsymbol{r}_{aj}$ are positions of atoms in the unit cell) and thus $g^*(-\boldsymbol{k}) = g(\boldsymbol{k})$. Then we have

$$h_{\boldsymbol{k}} = \begin{pmatrix} \xi_1(\boldsymbol{k}) & \Delta_1(\boldsymbol{k}) & g(\boldsymbol{k}) & 0 \\ \Delta_1^*(\boldsymbol{k}) & -\xi_1(\boldsymbol{k}) & 0 & -g(\boldsymbol{k}) \\ g^*(\boldsymbol{k}) & 0 & \xi_2(\boldsymbol{k}) & \Delta_2(\boldsymbol{k}) \\ 0 & -g^*(\boldsymbol{k}) & \Delta_2^*(\boldsymbol{k}) & -\xi_2(\boldsymbol{k}) \end{pmatrix}. \tag{S22}$$

For this 2-band model the trace indicated in Eq. (S15) can be explicitly performed. This leads to the following expression for the Hall conductivity

$$\sigma_H(\omega) = \frac{\mathrm{i}e^2}{2\omega\beta} \sum_{\boldsymbol{k},\omega_n} \frac{2\nu_m(\nu_m + 2\omega_n)}{\left(E_-^2 + \omega_n^2\right)\left(E_+^2 + \omega_n^2\right)} \frac{(A+B)}{\left[E_-^2 + (\nu_m + \omega_n)^2\right]\left[E_+^2 + (\nu_m + \omega_n)^2\right]}\Bigg|_{\nu_m \to \omega + i\epsilon} \tag{S23}$$

where

$$\begin{aligned} A &= E_+(W - E_- X)\left[|g|^2 + \omega_n(\nu_m + \omega_n) - E_1 E_2\right] - W(E_1|\Delta_2|^2 + E_2|\Delta_1|^2) + \mathrm{Im}[\Delta_1^*\Delta_2]U(\nu_m + 2\omega_n), \\ B &= X\left\{\mathrm{Re}\left[E_+E_-\Delta_1\Delta_2^* + \Delta_1^*\Delta_2^*(\Delta_1^2 - \Delta_2^2)\right] + (|\Delta_1|^2 - |\Delta_2|^2)\left[|g|^2 - \omega_n(\nu_m + \omega_n) + E_1E_2\right]\right\}, \end{aligned} \tag{S24}$$

with

$$X = (\partial_{\boldsymbol{k}} g \times \partial_{\boldsymbol{k}} g^*)_z = 2\mathrm{i}\,\mathrm{Im}[\partial_{k_x} g \partial_{k_y} g^*], \quad W = 2\mathrm{i}\,(\delta\boldsymbol{v} \times \mathrm{Im}[g^*\partial_{\boldsymbol{k}} g])_z\,, \quad U = \left(\delta\boldsymbol{v} \times \partial_{\boldsymbol{k}}|g|^2\right)_z.$$

We defined the velocity anisotropy of the single-particle spectrum $\delta\boldsymbol{v} = \partial_{\boldsymbol{k}}(\xi_2 - \xi_1)$ and $E_\pm = E_1 \pm E_2$ with $E_{1,2}$ the positive eigenvalues of $h_{\boldsymbol{k}}$. Here the energy denominators come from $\det G_0^{-1}(\boldsymbol{k}, \omega_n) = \left(E_-^2 + \omega_n^2\right)\left(E_+^2 + \omega_n^2\right)$. Performing the requisite fermionic frequency summation and the analytic continuation leads to Eq. (7) shown in the main text.

[1] J Hwang, T Timusk, and G D Gu, "Doping dependent optical properties of $bi_2sr_2cacu_2o_8 + \delta$," Journal of Physics: Condensed Matter **19**, 125208 (2007).

[2] Oguzhan Can, Tarun Tummuru, Ryan P. Day, Ilya Elfimov, Andrea Damascelli, and Marcel Franz, "High-temperature topological superconductivity in twisted double-layer copper oxides," Nature Physics (2021), 10.1038/s41567-020-01142-7.

[3] Edward Taylor and Catherine Kallin, "Intrinsic hall effect in a multiband chiral superconductor in the absence of an external magnetic field," Phys. Rev. Lett. **108**, 157001 (2012)